

Tensor-Product Bitstring Selected Configuration Interaction

Enhua Xu,^{1,*} William Dawson,¹ Himadri Pathak,^{2,1} and Takahito Nakajima¹

¹RIKEN Center for Computational Science, Kobe, Japan

²RIKEN Center for Interdisciplinary Theoretical and Mathematical Sciences, Wako, Japan

We present tensor-product bitstring selected configuration interaction (TBSCI), the first SCI approach with fully distributed CI vector storage enabled by a tensor-product bitstring representation. Coupled with a novel bitstring-based algorithm and scalable MPI communication strategies, TBSCI handles 2.6 trillion determinants on Fugaku—doubling the largest full CI calculation and exceeding the previous SCI record by over three orders of magnitude. Based on our bitstring selection, TBSCI achieves near-full CI accuracy with only a tiny fraction of the Hilbert space, establishing a scalable and physically grounded framework for large-scale SCI simulations.

Simulating strongly correlated quantum systems remains a central challenge in quantum many-body physics, with implications across quantum chemistry, materials science, and quantum information. Full configuration interaction (FCI) [1–5] provides exact solutions within a finite basis, but scales exponentially, limiting its application to few-electron systems. The FCI wavefunction can be expressed as $|\Psi_{\text{FCI}}\rangle = \sum_{K=1}^{N_{\text{FCI}}} c_K |D_K\rangle$, where N_{FCI} is the total number of determinants in FCI, and $|D_K\rangle$ is a Slater determinant with variational coefficient c_K . Selected configuration interaction (SCI) methods [6–9] approximate the FCI wavefunction by selecting only important determinants—typically those with significant estimated energy contributions or coefficients.

Since each determinant can be factorized into a tensor-product of an α - and a β -bitstring, $|D_K\rangle = |S_w^\alpha\rangle \otimes |S_u^\beta\rangle$, the FCI wavefunction can equivalently be written as

$$|\Psi_{\text{FCI}}\rangle = \sum_{w=1}^{L_\alpha} \sum_{u=1}^{L_\beta} c_{(w,u)} |S_w^\alpha\rangle \otimes |S_u^\beta\rangle, \quad (1)$$

where L_α and L_β denote the total numbers of α - and β -bitstrings in FCI. Since $L_\alpha, L_\beta \ll N_{\text{FCI}}$, this tensor-product bitstring (TPB) structure motivates selecting important bitstrings rather than important determinants directly. We refer to this approach as tensor-product bitstring SCI (TBSCI).

As an extension of the quantum SCI (QSCI) strategy [10], an IBM team recently introduced the TPB structure into SCI to restore spin symmetry (S^2) in noisy quantum wavefunctions [11]. While their work employed the TPB form as a tool for quantum error mitigation, we instead identify it as a physically motivated structure of the FCI wavefunction itself, as expressed in Eq. (1), and propose a bitstring selection strategy based on $|c_{(w,u)}|$ values above a chosen threshold—analogous to traditional SCI’s use of $|c_K|$.

Despite advances in determinant selection and perturbative corrections [7–9, 12–17], SCI methods remain fundamentally constrained by the size of the CI matrix that can be diagonalized. This limitation arises from the use of fully replicated CI vectors, which restricts the CI vector dimension to the memory capacity of a single node.

To overcome this bottleneck, we implement distributed matrix-vector multiplication over distributed CI vector storage, develop a novel algorithm tailored for TBSCI, and design a suite of MPI communication strategies to reduce congestion and improve scalability. We devote substantial attention to the design and performance of distributed CI vector handling, as it is a prerequisite for any scalable implementation of SCI.

Distributed CI Vector Storage: In TBSCI, the selected α - and β -bitstrings are denoted as S_w^α and S_u^β , with $w = 1, \dots, l_\alpha$ and $u = 1, \dots, l_\beta$, where l_α and l_β are the number of selected α - and β -bitstrings. Determinants are globally indexed by $K = (w-1)l_\beta + u$. This corresponds to a (β, α) -lexicographic ordering, with β varying fastest.

As illustrated in Fig. 1, we distribute the large CI vector across MPI processes by partitioning the α -bitstrings. Each process p holds m_p such bitstrings and stores $m_p \times l_\beta$ coefficients, ensuring balanced memory usage. The determinant structure itself requires no explicit storage, as indices suffice.

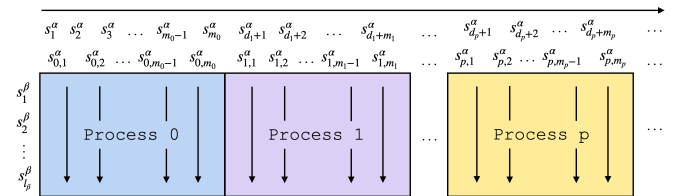


FIG. 1. Distribution of the CI vector into segments across N processes. Each process holds a strict subset of m_p α -bitstrings. On a local process, the determinants are divided into segments (indicated by vertical arrows), where each segment contains all determinants sharing the same α -bitstring. For this figure, we define a displacement index $d_p = \sum_{i=0}^{p-1} m_i$ to indicate the offset of α -bitstrings assigned to each process.

Distributed Matrix-Vector Multiplication: CI eigenstates are computed via Davidson diagonalization [18], the cost of which is dominated by the evaluation of $\mathbf{W} = \mathbf{H} \cdot \mathbf{U}$. Unlike replicated-vector implementations, each process p stores only its assigned CI vector segment, \mathbf{U}_p , and computes its local contribution, \mathbf{W}_p , according

to

$$\mathbf{W}_p = \sum_q H \cdot \mathbf{U}_q. \quad (2)$$

Each Davidson iteration consists of N asynchronous *steps* per process, each involving a one-sided MPI_GET and accumulation of $H \cdot \mathbf{U}_q$. Communication and computation are overlapped: one thread handles data transfer for the next step, while others perform OpenMP-parallel matrix-vector operations for the current step. We define the step delay as $t_{\text{delay}} = \max(0, t_{\text{data}} - t_{\text{cal}})$, where t_{data} and t_{cal} denote the data retrieval time and computation time during the current step, respectively; the total delay of one Davidson iteration is thus $T_{\text{delay}} = \sum t_{\text{delay}}$. A mixed-precision implementation, in which matrix-vector multiplication is performed in single precision, reduces communication volume and significantly lowers T_{delay} .

Efficient Hamiltonian Computation: Due to the Slater–Condon rules, the Hamiltonian matrix H is highly sparse, with nonzero elements only when the bitstring differences satisfy $\text{DIFF}(S_w^\alpha, S_x^\alpha) + \text{DIFF}(S_u^\beta, S_v^\beta) \leq 2$. We classify valid Hamiltonian terms into six (a, b) excitation classes, where a and b are the numbers of orbital differences in the α and β strings, respectively. All off-diagonal elements $([2, 0], [1, 1], [1, 0], [0, 2], [0, 1])$ are computed on-the-fly; diagonal terms $([0, 0])$ are precomputed for efficiency.

By exploiting the TPB structure to evaluate H on-the-fly, we propose the bitstring-based Algorithm 1 for computing $\mathbf{W}_p += H \cdot \mathbf{U}_q$. The **SINGLE_LINK** and **DOUBLE_LINK** arrays store the β -bitstring connections for single and double excitations, respectively. Considering the sparsity of both single and double excitations can be estimated as $\sqrt{N_{\text{TBSCI}}/N_{\text{FCI}}}$ (N_{TBSCI} is the number of determinants in TBSCI), the memory usage for **SINGLE_LINK** and **DOUBLE_LINK** scale as $l_\beta N_{\text{occ}} N_{\text{vir}} \sqrt{N_{\text{TBSCI}}/N_{\text{FCI}}}$ and $l_\beta N_{\text{occ}}^2 N_{\text{vir}}^2 \sqrt{N_{\text{TBSCI}}/N_{\text{FCI}}}$, respectively, for N_{occ} occupied and N_{vir} virtual orbitals. **DOUBLE_LINK** is distributed across processes in batches to reduce memory usage, while **SINGLE_LINK** is replicated for fast access. Owing to the fixed β -strings associated with each α -string, which enables efficient reuse of precomputed excitation patterns, this structure minimizes both memory and communication overhead during Hamiltonian evaluation. The overall computational scaling of TBSCI is $N_{\text{TBSCI}} N_{\text{occ}}^2 N_{\text{vir}}^2 \sqrt{N_{\text{TBSCI}}/N_{\text{FCI}}}$.

Execution Strategies for Distributed TBSCI: Distributing the CI vector enables large-scale calculations beyond single-node memory limits but introduces multi-step execution and potential MPI congestion. As the number of nodes increases, communication overhead can dominate and degrade scalability. To address this challenge, we implement a suite of MPI optimization strategies that are critical for mitigating congestion and achiev-

Algorithm 1: Local computation of matrix elements on process p at step q .

Data: current process p , current step q ;
SINGLE_LINK and **DOUBLE_LINK** lists

```

1 for  $S_w^\alpha \leftarrow S_{p,1}^\alpha$  to  $S_{p,m_p}^\alpha$  do
2   for  $S_x^\alpha \leftarrow S_{q,1}^\alpha$  to  $S_{q,m_q}^\alpha$  do
3     case  $\leftarrow \text{DIFF}(S_w^\alpha, S_x^\alpha)$ 
4     if case = 2 then
5       for  $S_u^\beta \leftarrow S_1^\beta$  to  $S_{l_\beta}^\beta$  do
6          $S_v^\beta \leftarrow S_u^\beta$ 
7         Calculate [2,0] term
8       end for
9     else if case=1 then
10      for  $S_u^\beta \leftarrow S_1^\beta$  to  $S_{l_\beta}^\beta$  do
11        foreach  $S_v^\beta \in \text{SINGLE\_LINK}(:, S_u^\beta)$  do
12          Calculate [1,1] term
13        end foreach
14         $S_v^\beta \leftarrow S_u^\beta$ 
15        Calculate [1,0] term
16      end for
17    else if case=0 then
18      for  $S_u^\beta \leftarrow S_1^\beta$  to  $S_{l_\beta}^\beta$  do
19        foreach  $S_v^\beta \in \text{SINGLE\_LINK}(:, S_u^\beta)$  do
20          Calculate [0,1] term
21        end foreach
22         $S_v^\beta \leftarrow S_u^\beta$ 
23        Calculate [0,0] term
24      end for
25    end if
26  end for
27   $S_x^\alpha \leftarrow S_w^\alpha$ 
28  foreach  $S_u^\beta \in$  the  $q$ -th batch of  $\{S^\beta\}$  do
29    foreach  $S_v^\beta \in \text{DOUBLE\_LINK}(:, S_u^\beta)$  do
30      Calculate [0,2] term
31    end foreach
32  end foreach
33 end for

```

ing high parallel efficiency at scale (as detailed in **End Matter**).

Scalability and Parallel Efficiency: We evaluated TBSCI scalability by computing FCI energies for N_2 (aug-cc-pVDZ) and CN (cc-pVTZ) potential energy surfaces (PESs), as well as single-point energies of Cr_2 (STO-3G) and N_2 (cc-pVTZ) near equilibrium. Specifically, the FCI dimensions (including frozen-core orbitals and molecular symmetry) are 1.47×10^{11} for N_2 (aug-cc-pVDZ, D_{2h} symmetry, 2 frozen orbitals), 4.86×10^{11} for CN (cc-pVTZ, C_{2v} symmetry, 2 frozen orbitals), 9.14×10^{11} for Cr_2 (STO-3G, D_{2h} symmetry, 12 frozen orbitals), and 2.62×10^{12} for N_2 (cc-pVTZ, D_{2h} symmetry, 2 frozen orbitals). The Hartree–Fock (HF) reference states and corresponding FCIDUMP files were generated using PySCF [19]. Calculations were performed entirely in memory, eliminating disk I/O and enabling fast CI updates.

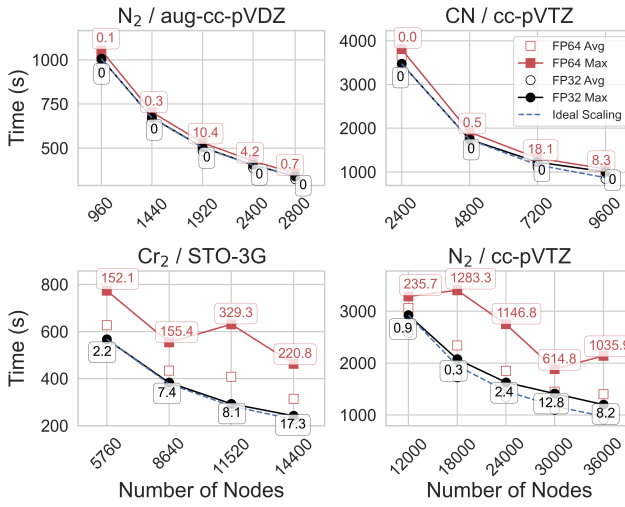


FIG. 2. Wall time (in seconds) for a single distributed matrix–vector multiplication across four benchmark systems using double-precision (FP64) and mixed-precision (FP32) implementations. Solid lines represent the average and maximum wall times across nodes, while dashed lines indicate ideal scaling relative to the smallest-node run. Red and black markers correspond to FP64 and FP32 results, respectively. Small boxed labels indicate T_{delay} on the slowest process.

Figure 2 shows the wall time of a single distributed matrix–vector multiplication—the dominant cost in Davidson diagonalization—across node counts for all systems. Detailed timings and node-hour costs are provided in Table III in **End Matter**. Due to limited computational resources, we report the value of T_{delay} from the first test run rather than the average over multiple runs. The mixed-precision (FP32) implementation consistently reduces communication delays (T_{delay}), maintaining zero delay below 5,000 nodes and remaining under 18 s even at 36,000 nodes (1.7 million cores). In contrast, double precision (FP64) shows significantly larger delays: up to 18.1 s (CN), 329.3 s (Cr₂), and 1283.3 s (N₂, cc-pVTZ).

T_{delay} variability across runs further highlights this effect. FP32 yields small, relatively consistent delays in Cr₂ and N₂(cc-pVTZ), whereas FP64 shows high variance and occasional extreme delays. These trends confirm that reduced data volume in FP32 significantly mitigates MPI congestion. Since $t_{\text{delay}} = t_{\text{data}} - t_{\text{cal}}$, performance may vary with machine architecture; faster CPUs with similar interconnects could increase T_{delay} , while faster networks should benefit FP64. Thus, FP32’s strong performance reflects both its compute–communication balance on Fugaku and our communication-optimized design.

FP32 also achieves better parallel performance: its max-to-avg wall time ratio is $\sim 20\%$ lower than FP64 in Cr₂ and N₂ (cc-pVTZ), indicating improved load balance. This leads to higher strong scaling efficiency—for

Cr₂ and N₂ (cc-pVTZ), FP32 retains over 93% and 80% efficiency at 14,400 and 36,000 nodes, respectively, while FP64 drops to 67% and 51%. These results confirm the scalability and robustness of the FP32 implementation and the associated MPI strategies.

TBSCI Based on FCI-Derived Bitstrings: In addition to single-iteration benchmarks, we ran all systems to convergence (energy change below 10^{-7} Hartree) to obtain final FCI energies and amplitudes. Despite single-precision matrix–vector operations in FP32, energy deviations from FP64 remained below 2×10^{-6} Hartree for all systems, except N₂ (cc-pVTZ), which was computed only in FP32 due to excessive T_{delay} at large scale. Thus, only FP32 results are reported, rounded to five decimal places.

TABLE I. Summary of TBSCI results for N₂ (aug-cc-pVDZ) along the potential energy surface (PES) using FCI-derived bitstrings. All energy differences $E_{\text{TBSCI}} - E_{\text{FCI}}$ are in millihartree (mH). Bond lengths R are in Bohr.

c_{relative}	$N_{\text{bitstrings}}$	N_{TBSCI}	$N_{\text{TBSCI}}/N_{\text{FCI}}$	ΔE (mH)
$R = 2.068$ a.u., $E_{\text{HF}} = -108.96104$, $E_{\text{FCI}} = -109.29526$				
1×10^{-3}	812	328,434	0.00022%	23.77
6×10^{-4}	1,106	511,050	0.00035%	18.88
3×10^{-4}	1,991	1,083,255	0.00074%	13.06
$R = 2.4$ a.u., $E_{\text{HF}} = -108.87532$, $E_{\text{FCI}} = -109.25893$				
1×10^{-3}	1,022	381,188	0.00026%	24.63
6×10^{-4}	1,523	690,073	0.00047%	18.64
3×10^{-4}	2,990	1,959,794	0.0013%	11.72
$R = 2.7$ a.u., $E_{\text{HF}} = -108.74804$, $E_{\text{FCI}} = -109.18216$				
1×10^{-3}	1,262	459,468	0.00031%	25.21
6×10^{-4}	1,973	972,333	0.00066%	18.73
3×10^{-4}	3,851	2,962,705	0.0020%	11.35
$R = 3.0$ a.u., $E_{\text{HF}} = -108.61893$, $E_{\text{FCI}} = -109.10879$				
1×10^{-3}	1,597	626,443	0.00043%	26.01
6×10^{-4}	2,578	1,458,224	0.00099%	18.63
3×10^{-4}	5,024	4,631,324	0.0031%	11.14
$R = 3.6$ a.u., $E_{\text{HF}} = -108.40128$, $E_{\text{FCI}} = -109.01633$				
1×10^{-3}	3,126	1,668,780	0.0011%	22.82
6×10^{-4}	4,881	3,920,037	0.0027%	15.50
3×10^{-4}	8,842	11,864,568	0.0080%	9.26
$R = 4.2$ a.u., $E_{\text{HF}} = -108.24292$, $E_{\text{FCI}} = -108.96604$				
1×10^{-3}	5,058	3,744,434	0.0025%	15.50
6×10^{-4}	7,648	8,325,888	0.0056%	11.42
3×10^{-4}	13,430	24,827,776	0.017%	7.14

To accommodate system-dependent amplitude distributions, we selected important determinants based on relative coefficients $|c_{(w,u)}/c_{\text{HF}}|$, rather than absolute values. Determinants with $|c_{(w,u)}/c_{\text{HF}}| > \delta$ were used to extract the corresponding α - and β -bitstrings for constructing the TBSCI determinant set. Varying δ yields different sets of determinants and corresponding TBSCI

energies, which are directly compared with FCI results in Tables I and II.

Table I reports TBSCI results for N_2 (aug-cc-pVDZ) at thresholds $\delta = 10^{-3}$, 6×10^{-4} , and 3×10^{-4} . Despite the transition from single- to multi-reference character along the PES, TBSCI energies remain within 11–23 $\text{m}E_h$ of FCI using as little as 0.003% of the FCI determinants. Moreover, the deviation remains stable along the PES, approximately 23, 17, and 11 $\text{m}E_h$ for $\delta = 10^{-3}$, 6×10^{-4} , and 3×10^{-4} , respectively. This robustness highlights the effectiveness of relative-amplitude screening.

The same strategy was applied to CN, Cr_2 , and N_2 (cc-pVTZ) as shown in Table II. Several PES geometries of CN were selected. In all systems, TBSCI recovers near-FCI accuracy with very small $N_{\text{TBSCI}}/N_{\text{FCI}}$ ratios; although for the transition metal Cr_2 , this ratio is higher. Such performance suggests that key determinants arise from combinations of important α - and β -bitstrings, while others contribute little. The FCI energies of CN with cc-pVDZ, cc-pVTZ, and complete basis set (CBS) extrapolation along the PES are listed in Table IV in **End Matter**.

Although developed independently, our bitstring selection strategy bears conceptual similarity to a 2008 proposal by Surján *et al.* [12], which we restate here as

$$W(S_x) = \sum_{K \in \mathcal{K}(S_x)} \frac{(\langle D_K | \hat{H} - E | \Psi \rangle)^2}{E - E_K}, \quad (3)$$

where $\mathcal{K}(S_x)$ denotes the set of determinants containing S_x as their α - or β -component. $W(S_x)$ quantifies the importance of bitstring S_x as the sum of approximate energy contributions from all related determinants. Since the terms in Eq. (3) often differ by orders of magnitude, the summation may be well approximated by its largest term, implying that important bitstrings can be identified by estimating contributions from individual important determinants. While this analysis resembles the Heat-bath algorithm in SHCI [8]—which approximates a summation by its maximum term—a key difference is that Eq. (3) involves only positive terms, whereas the SHCI summation contains both positive and negative contributions. In practical applications, since exact FCI amplitudes are unavailable, important determinants must be identified using estimated amplitudes, so further validation of our bitstring selection strategy across diverse systems is warranted.

Here, we report the first scalable SCI implementation featuring fully distributed CI vector storage. By exploiting the TPB structure—naturally compatible with distributed memory architectures—we devised a novel bitstring-based algorithm coupled with MPI communication optimizations tailored to TBSCI. Our implementation efficiently handles 2.62×10^{12} determinants on over 1.7 million cores of Fugaku, surpassing the scale of the largest FCI calculation to date [5] (1.31×10^{12} deter-

TABLE II. Summary of TBSCI results for CN (cc-pVTZ), Cr_2 (STO-3G), and N_2 (cc-pVTZ) using FCI-derived bitstrings. For the open-shell CN system, the numbers of selected α - and β -bitstrings (l_α and l_β) are listed separately as l_α/l_β . All energy differences $E_{\text{TBSCI}} - E_{\text{FCI}}$ are in millihartree (mH). Bond lengths R are given in Å, except for N_2 , where $R = 2.068$ a.u. (≈ 1.094 Å) to match the PES in Table I.

δ	$N_{\text{bitstrings}}$	N_{TBSCI}	$N_{\text{TBSCI}}/N_{\text{FCI}}$	ΔE (mH)
CN, $R = 1.116$ Å, $E_{\text{HF}} = -92.21949$, $E_{\text{FCI}} = -92.56925$				
1×10^{-3}	1227/991	760,395	0.00016%	28.23
6×10^{-4}	1923/1516	1,765,756	0.00036%	20.07
3×10^{-4}	3443/2597	4,526,671	0.00093%	12.81
Cr_2 , $R = 1.5$ Å, $E_{\text{HF}} = -92.05959$, $E_{\text{FCI}} = -92.47605$				
1×10^{-3}	1354/1014	700,406	0.00014%	31.14
6×10^{-4}	2328/1672	1,917,168	0.00039%	21.01
3×10^{-4}	4465/3096	5,889,944	0.0012%	12.22
CN, $R = 2.0$ Å, $E_{\text{HF}} = -91.84459$, $E_{\text{FCI}} = -92.32482$				
1×10^{-3}	3357/1770	1,880,028	0.00039%	23.71
6×10^{-4}	5481/2920	5,026,408	0.0010%	15.39
3×10^{-4}	10637/5271	16,978,381	0.0014%	8.35
N_2 , $R = 1.5$ Å, $E_{\text{HF}} = -2064.07890$, $E_{\text{FCI}} = -2064.80819$				
1×10^{-3}	4307	2,453,517	0.00027%	43.87
6×10^{-4}	7104	6,341,246	0.00069%	30.69
3×10^{-4}	14345	25,875,325	0.0028%	17.91
2×10^{-4}	21655	58,896,667	0.0064%	12.37
1×10^{-4}	40233	203,880,331	0.022%	6.54
N_2 , $R = 2.068$ a.u., $E_{\text{HF}} = -108.98409$, $E_{\text{FCI}} = -109.37515$				
1×10^{-3}	951	904,401	0.000034%	30.07
6×10^{-4}	1455	2,117,025	0.000081%	22.66
3×10^{-4}	2678	7,171,684	0.00027%	15.35
2×10^{-4}	3985	15,880,225	0.00061%	11.65
1×10^{-4}	8395	70,476,025	0.0027%	6.37

nants) and exceeding the previous SCI record [15] (2×10^9 determinants) by over three orders of magnitude.

This work reveals the intrinsic compactness of the TPB structure for representing FCI wavefunctions: by leveraging FCI-derived bitstrings, TBSCI achieves near-FCI accuracy using only a tiny fraction of the Hilbert space across all tested systems. This implies that important determinants are largely constructed from a small number of important α - and β -bitstrings. Consequently, selecting determinants via bitstring spaces L_α and L_β , which are orders of magnitude smaller than the FCI space, offers a physically motivated and computationally efficient route for SCI. Combined with our scalable bitstring-based infrastructure, TBSCI unlocks trillion-determinant simulations and paves the way for constructing compact CI spaces. Future work will integrate bitstring selection and perturbative corrections to extend TBSCI’s applicability to larger, more challenging systems.

ACKNOWLEDGMENTS

The authors acknowledge Muneaki Kamiya for proposing the subspace restart strategy in the Davidson algorithm, which helped reduce memory usage.

DATA AVAILABILITY

Input files and representative output data are available from the corresponding author upon a reasonable request.

* enhuaxu@riken.jp

- [1] P. J. Knowles and N. C. Handy, A new determinant-based full configuration interaction method, *Chem. Phys. Lett.* **111**, 315 (1984).
- [2] R. Ansaloni, G. L. Bendazzoli, S. Evangelisti, and E. Rossi, A parallel Full-CI algorithm, *Comput. Phys. Commun.* **128**, 496 (2000).
- [3] Z. Gan, Y. Alexeev, M. S. Gordon, and R. A. Kendall, The parallel implementation of a full configuration interaction program, *J. Chem. Phys.* **119**, 47 (2003).
- [4] B. S. Fales and B. G. Levine, Nanoscale multireference quantum chemistry: Full configuration interaction on graphical processing units, *J. Chem. Theory Comput.* **11**, 4708 (2015).
- [5] H. Gao, S. Imamura, A. Kasagi, and E. Yoshida, Distributed implementation of full configuration interaction for one trillion determinants, *J. Chem. Theory Comput.* **20**, 1185 (2024).
- [6] B. Huron, J. P. Malrieu, and P. Rancurel, Iterative perturbation calculations of ground and excited state energies from multiconfigurational zeroth-order wavefunctions, *J. Chem. Phys.* **58**, 5745 (1973).
- [7] N. M. Tubman, J. Lee, T. Y. Takeshita, M. Head-Gordon, and K. B. Whaley, A deterministic alternative to the full configuration interaction quantum monte carlo method, *J. Chem. Phys.* **145**, 044112 (2016).
- [8] A. A. Holmes, N. M. Tubman, and C. J. Umrigar, Heat-bath configuration interaction: An efficient selected configuration interaction algorithm inspired by heat-bath sampling, *J. Chem. Theory Comput.* **12**, 3674 (2016).
- [9] W. Liu and M. R. Hoffmann, iCI: Iterative CI toward full CI, *J. Chem. Theory Comput.* **12**, 1169 (2016).
- [10] K. Kanno, M. Kohda, R. Imai, S. Koh, K. Mitarai, W. Mizukami, and Y. O. Nakagawa, Quantum-selected configuration interaction: Classical diagonalization of hamiltonians in subspaces selected by quantum computers, *arXiv preprint* (2023), [arXiv:2302.11320](https://arxiv.org/abs/2302.11320).
- [11] J. Robledo-Moreno, M. Motta, H. Haas, A. Javadi-Abhari, P. Jurcevic, W. Kirby, S. Martiel, K. Sharma, S. Sharma, T. Shirakawa, I. Sitzdikov, R. Sun, K. J. Sung, M. Takita, M. C. Tran, S. Yunoki, and A. Mezzacapo, Chemistry beyond the scale of exact diagonalization on a quantum-centric supercomputer, *Sci. Adv.* **11**, eadu9991 (2025).
- [12] Z. Rolik, Á. Szabados, and P. R. Surján, A sparse matrix based full-configuration interaction algorithm, *J. Chem. Phys.* **128**, 144101 (2008).
- [13] D. B. Williams-Young, N. M. Tubman, C. Mejuto-Zaera, and W. A. de Jong, A parallel, distributed memory implementation of the adaptive sampling configuration interaction method, *J. Chem. Phys.* **158**, 214109 (2023).
- [14] S. Sharma, A. A. Holmes, G. Jeanmairet, A. Alavi, and C. J. Umrigar, Semistochastic heat-bath configuration interaction method: Selected configuration interaction with semistochastic perturbation theory, *J. Chem. Theory Comput.* **13**, 1595 (2017).
- [15] J. Li, M. Otten, A. A. Holmes, S. Sharma, and C. J. Umrigar, Fast semistochastic heat-bath configuration interaction, *J. Chem. Phys.* **149**, 214110 (2018).
- [16] N. Zhang, W. Liu, and M. R. Hoffmann, Iterative configuration interaction with selection, *J. Chem. Theory Comput.* **16**, 2296 (2020).
- [17] N. Zhang, W. Liu, and M. R. Hoffmann, Further development of iCIPT2 for strongly correlated electrons, *J. Chem. Theory Comput.* **17**, 949 (2021).
- [18] E. R. Davidson, The iterative calculation of a few of the lowest eigenvalues and corresponding eigenvectors of large real-symmetric matrices, *J. Comput. Phys.* **17**, 87 (1975).
- [19] Q. Sun, T. C. Berkelbach, N. S. Blunt, G. H. Booth, S. Guo, Z. Li, J. Liu, J. D. McClain, E. R. Sayfutyarova, S. Sharma, S. Wouters, and G. K.-L. Chan, Pyscf: the python-based simulations of chemistry framework, *Wiley Interdiscip. Rev. Comput. Mol. Sci.* **8**, e1340 (2018).

END MATTER

MPI Communication Optimization Strategies

1. Avoiding unnecessary MPI data transfers. As described in Eq. (2), each process p must retrieve CI vector segments from other processes during distributed matrix–vector multiplication. However, not all remote segments are required for local Hamiltonian evaluation. Specifically, for any remote α -bitstring S_x^α , if all local α -bitstrings $\{S_{p,1}^\alpha, \dots, S_{p,m_p}^\alpha\}$ satisfy $\text{DIFF}(S_{p,i}^\alpha, S_x^\alpha) > 2$, then the segment corresponding to S_x^α can be safely omitted. This excitation-connectivity information is precomputed and stored, allowing each process to bypass unnecessary data transfers and thereby reduce MPI communication volume to scale approximately with the local computational workload.

Molecular symmetry further reduces data volume: if $\text{DIFF}(S_w^\alpha, S_x^\alpha) = 2$ and S_w^α and S_x^α belong to different symmetry sectors, the corresponding Hamiltonian matrix elements vanish, eliminating the need to fetch those segments. For instance, enforcing D_{2h} symmetry reduces memory usage by a factor of ~ 8 , and communication and computational costs by a factor of ~ 64 . With symmetry adaptation, the determinant space no longer forms a simple tensor product of independently chosen α - and β -bitstrings; only symmetry-allowed combinations and operations are retained. For completeness and clarity, however, we retain the full algorithmic forms in the manuscript.

2. Minimizing long-distance MPI communication. Each node is assigned a unique ID from 0 to $N - 1$. Since messages between nodes with nearby IDs traverse fewer network hops (when suitably ordered), we sort α -bitstrings by their excitation levels relative to the Hartree–Fock (HF) determinant and assign them to nodes in ascending order. Lower-excitation bitstrings are placed on lower-numbered nodes, while higher-excitation ones are assigned to higher-numbered nodes. Because excitation differences between distant bitstrings often exceed two, data retrieval from remote nodes is frequently unnecessary. This excitation-aware mapping ensures that, even on tens of thousands of nodes, each node primarily fetches CI vector segments from its nearest neighbors, thereby mitigating MPI congestion and sustaining high parallel efficiency.

3. Balancing memory and computational load. Algorithm 1 allows estimation of computational costs associated with each α -bitstring segment. The total workload of a process is approximated by summing the costs of its assigned bitstrings. While α -bitstrings are assigned in ascending excitation order, balancing memory usage and computational load simultaneously is challenging. We define two expansion factors: the memory expansion factor (the ratio of assigned bitstring count to the average)

and the computation expansion factor (the ratio of estimated cost to the average). Strictly enforcing memory balance (memory factor ≈ 1) risks severe computational imbalance, causing idle processes, whereas strictly enforcing computational balance (computation factor ≈ 1) may overload memory on some nodes. We therefore adopt a compromise strategy, maintaining both factors moderately above one to balance memory and computation effectively. For FCI calculations, where per-segment costs are uniform, a uniform distribution naturally balances both aspects.

4. Absorbing delays via reassignment of [0, 2] tasks. The $[0, 2]$ terms (double excitations within the β -bitstring space) are evaluated independently in a separate batch loop (lines 27–32 in Algorithm 1), enabling flexible workload distribution. Each process estimates the computational workload of its N steps based on assigned α -bitstrings and redistributes its N batches of $[0, 2]$ tasks accordingly, assigning more tasks to steps with smaller pre-estimated workloads. These $[0, 2]$ tasks serve as a computational reservoir, mitigating delays (t_{delay}) caused by imbalances between data transfer (t_{data}) and computation (t_{cal}). Steps requiring no data retrieval (when excitation differences exceed two) can be eliminated after reassignment. While this breaks the strict one-step-one-batch structure, the original form is maintained for clarity.

5. Odd-even process fetch ordering. Simultaneous MPI data transfers can cause network congestion spikes. To alleviate this issue, the target ranks are sorted by the number of required segments. Odd-numbered processes fetch data in ascending order, while even-numbered processes fetch in descending order. This simple approach effectively reduces both the frequency and magnitude of delay times, especially in large-scale runs with thousands of nodes.

6. “Check if busy” dynamic scheduling. When process A performs MPI_GET from process B, both are marked **BUSY**. Other processes preferentially fetch from **NOT BUSY** targets but can access **BUSY** ones if necessary. This dynamic scheduling reduces communication congestion and improves overall parallel efficiency.

7. Sleep strategy under severe MPI congestion. Despite prior optimizations, severe T_{delay} spikes occasionally occur in runs involving over ten thousand nodes, leading to cascading congestion akin to traffic jams. To mitigate this, if a process detects t_{delay} exceeding a specified threshold (e.g., 0.2 s), it enters a brief sleep period (e.g., 0.1 s), marking itself as **BUSY** during the sleep to discourage other processes from fetching data from the congested process. While this approach slightly increases T_{delay} within a single Davidson iteration, it consistently suppresses large delay spikes and improves stability in large-scale runs. Threshold values were empirically tuned on Fugaku and may require adjustment for other architectures or computational methods.

Details of the parallel performance

In Table III, we report detailed timings for the TBSCI calculations described in the main text.

TABLE III. Parallel performance of TBSCI for various molecules and basis sets using both double- (FP64) and mixed-precision (FP32) implementations. For each case, we report the average wall time (Avg.), maximum wall time (Max.), and delay time (T_{delay}) of the slowest process in a single distributed matrix-vector multiplication in seconds, as well as the total node hours (NHs) consumed.

<i>N₂</i> (aug-cc-p VDZ)								
#Nodes	FP64				FP32			
	Avg.	Max.	T_{delay}	NHs	Avg.	Max.	T_{delay}	NHs
960	1016	1053	0.1	281	968	1007	0	269
1440	676	704	0.3	282	645	673	0	269
1920	509	531	10.4	283	484	505	0	269
2400	407	426	4.2	284	387	405	0	270
2880	341	358	0.7	286	325	340	0	272
<i>CN</i> (cc-p VTZ)								
#Nodes	FP64				FP32			
	Avg.	Max.	T_{delay}	NHs	Avg.	Max.	T_{delay}	NHs
2400	3655	3809	0	2539	3331	3478	0	2319
4800	1824	1909	0.5	2545	1650	1743	0	2324
7200	1227	1315	18.1	2630	1110	1224	0	2448
9600	938	1070	8.3	2853	839	1003	0	2675
<i>Cr₂</i> (STO-3G)								
#Nodes	FP64				FP32			
	Avg.	Max.	T_{delay}	NHs	Avg.	Max.	T_{delay}	NHs
5760	627	774	152.1	1190	551	567	2.2	907
8640	434	554	155.4	1330	373	383	7.4	919
11520	408	631	329.3	2019	281	293	8.1	938
14400	314	463	220.8	1852	227	242	17.3	968
<i>N₂</i> (cc-p VTZ)								
#Nodes	FP64				FP32			
	Avg.	Max.	T_{delay}	NHs	Avg.	Max.	T_{delay}	NHs
12000	3063	3284	235.7	10947	2582	2924	0.1	9747
18000	2341	3403	1283.3	17015	1726	2076	0.3	10380
24000	1853	2749	1146.8	18327	1346	1630	2.4	10876
30000	1448	1886	614.8	15717	1102	1413	12.8	11775
36000	1402	2139	1035.9	21390	917	1201	8.2	12010

Potential Energy Surface of CN

Table IV reports the potential energy surface of the CN molecule computed using the cc-pVDZ and cc-pVTZ basis sets. We also include extrapolated values to the complete basis set (CBS) limit using standard two-point extrapolation formulas. The Hartree–Fock (HF) energy at a given cardinal number c is extrapolated using:

$$E_{\text{CBS}}^{\text{HF}}(l/m) = E_m^{\text{HF}} - \frac{(E_m^{\text{HF}} - E_l^{\text{HF}})m^{-5}}{m^{-5} - l^{-5}}, \quad (4)$$

and the correlation energy E^{Cor} as:

$$E_{\text{CBS}}^{\text{Cor}}(l/m) = E_m^{\text{Cor}} - \frac{(E_m^{\text{Cor}} - E_l^{\text{Cor}})m^{-3}}{m^{-3} - l^{-3}}. \quad (5)$$

All HF and FCI energies are reported in Hartree (E_h), computed in mixed precision. Differences between mixed- and double-precision values are below $2 \times 10^{-6} E_h$.

TABLE IV. Potential energy surface of CN computed with cc-pVDZ and cc-pVTZ basis sets, and extrapolated to the CBS limit. All energies are in Hartree (E_h).

R (Å)	cc-pVDZ		cc-pVTZ		CBS(2/3)
	HF	FCI	HF	FCI	FCI
1.16	-92.19762	-92.49181	-92.21949	-92.56925	-92.59597
1.30	-92.14998	-92.47936	-92.16834	-92.55025	-92.57515
1.50	-92.04171	-92.40866	-92.05959	-92.47605	-92.49961
1.70	-91.93773	-92.33464	-91.95735	-92.40074	-92.42329
2.00	-91.82229	-92.26205	-91.84459	-92.32482	-92.34524
2.30	-91.70416	-92.24217	-91.72723	-92.30050	-92.31885